Journal of Solid State Chemistry 184 (2011) 1381–1386

Contents lists available at ScienceDirect

Journal of Solid State Chemistry

journal homepage: www.elsevier.com/locate/jssc

Synthesis and crystal structure of two new cerium rhodium oxides: $Ce_{2/3-x}Rh_2^{3+}O_4$ ($x\sim0.12$) with Ce mixed valency and $Ce^{4+}Rh_2^{3+}O_5$

Hiroshi Mizoguchi [a], L.N. Zakharov [a], N.S.P. Bhuvanesh [b], A.W. Sleight [a], M.A. Subramanian [a,*]

[a] Department of Chemistry, Oregon State University, Corvallis, OR 97331-4003, USA
[b] Department of Chemistry, Texas A&M University, College Station, TX 77842-3012, USA

ARTICLE INFO

Article history:
Received 19 January 2011
Received in revised form
24 March 2011
Accepted 4 April 2011
Available online 12 April 2011

Keywords:
Rhodium oxides
Cerium
Crystal structure
Electrical properties

ABSTRACT

The new compounds $Ce_{2/3-x}Rh_2O_4$ ($x\sim0.11$–0.14) and $CeRh_2O_5$ have been prepared. Their structures were determined from single crystal X-ray diffraction data. Electrical and magnetic properties were also evaluated. Based on the structural analysis and physical properties, oxidation states for $CeRh_2O_5$ can be assigned as $Ce^{4+}Rh_2^{3+}O_5$. A small variation in x was detected for $Ce_{2/3-x}Rh_2O_4$ indicating a formula ranging from $Ce_{0.55}^{3.64+}Rh_2^{3+}O_4$ to $Ce_{0.525}^{3.81+}Rh_2^{3+}O_4$.

1. Introduction

Rhodium is commonly found as Rh^{3+} or Rh^{4+} in oxides [1]. Synthesis in air usually results in Rh^{3+}, which takes octahedral coordination. For many years only two structures have been known in *R*–Rh–O ternary systems (*R*=rare earth cation). One structure is perovskite-type $RRhO_3$ [2,3]. The other structure is pyrochlore-type $R_2Rh_2O_7$, which requires a high pressure synthesis [4]. Recently, $R_{2/3-x}Rh_2O_4$ phases with a defect $CaFe_2O_4$-type structure were reported [5]. We have now investigated the Ce–Rh–O system in search of new compounds. Although the most common oxidation state for rare earths in oxides is the trivalent state, for Ce we might expect either Ce^{3+} or Ce^{4+}.

2. Experimental

Reactants were CeO_2 nanopowder (99.9%, Aldrich), $Ce(NO_3)_3\cdot6H_2O$ (99.99%, Aldrich), PbO (99.9%, Aldrich), V_2O_5 (99.9%, Johnson Matthey), NaCl (99.9%, Mallinckrodt) and Rh_2O_3 prepared from $RhCl_3\times H_2O$ (99.9%, Alfa Aesar) by heating in moist air at 1073 K for 10 h. Single crystals of $CeRh_2O_5$ were grown in a flux of 66 mol% PbO and 33 mol% V_2O_5. An intimate mixture of polycrystalline CeO_2 (0.046 g), Rh_2O_3 (0.034 g), PbO (0.41 g), V_2O_5 (0.17 g) was heated to 1373 K under air in a covered alumina crucible. After holding for 10 h, the crucible was cooled to 973 K at a rate of 3 K/h. After reaching 973 K, it was cooled to room temperature at a rate of 300 K/h. The flux was dissolved in HNO_3(aq) at 360 K. For synthesis of the polycrystalline materials, appropriate amounts of CeO_2 (or $Ce(NO_3)_3\cdot6H_2O$) and Rh_2O_3 were mixed by grinding together under ethanol in an agate mortar. This pressed mixture was placed in an alumina boat and heated in air at 973, 1073, 1173, and 1373 K each for 10 h with intermediate grindings. Black powders resulted. The addition of NaCl as a flux was also tried. Single crystals of $Ce_{2/3-x}Rh_2O_4$ were grown in a mixture of $Ce(NO_3)_3\cdot6H_2O$ (0.037 g), Rh_2O_3 (0.044 g), and NaCl (0.5 g). The mixed powder was heated to 1273 K under air in a covered alumina crucible for 20 h. It was then cooled to room temperature at a rate of 300 K/h. The product consisted of lustrous black crystals about 0.1 mm in length.

The cationic compositions of the obtained single crystals were determined with a CAMECA SX100 electron microprobe analyzer. Single crystal X-ray diffraction data were collected on a Bruker SMART APEXII CCD system at 173 or 213 K. A standard focus tube was used with an anode power of 50 kV at 30 mA, a crystal to plate distance of 5.0 cm, 512 × 512 pixels/frame, beam center (256.52, 253.16), total frames of 6602, oscillation/frame of 0.50°, exposure/frame of 10.0 s/frame and SAINT integration. A subsequent SADABS correction was applied. Crystal structures were solved using the direct method program SHELXS and refined with the full-matrix least squares program SHELXTL [6]. Further details are given in Tables 1–3 and is available in cif files. X-ray powder diffraction patterns were obtained with a RIGAKU MINIFLEX II with Cu*K*α radiation and a graphite monochromator. VALENCE software was used to calculate bond valences [7].

* Corresponding author. Fax: +1 541 737 2062.
E-mail address: mas.subramanian@oregonstate.edu (M.A. Subramanian).

0022-4596/$ - see front matter © 2011 Elsevier Inc. All rights reserved.
doi:10.1016/j.jssc.2011.04.005

Table 1
Crystal data and structure refinement for $CeRh_2O_5$ and $Ce_{0.55}Rh_2O_4$.

Empirical formula	$CeRh_2O_5$	$Ce_{0.55}Rh_2O_4$
FW	425.94	347.59
T (K)	173(2)	213(2)
Wavelength (Å)	0.71073	0.71073
Crystal system	Orthorhombic	Orthorhombic
Space group	*Pnma*	*Pnma*
Unit cell dimensions (Å)	$a=7.1440(6)$	$a=9.014(13)$
	$b=9.8169(9)$	$b=3.055(5)$
	$c=5.0983(5)$	$c=10.812(16)$
Volume (Å^3)	357.55(6)	297.7(8)
Z	4	4
Density (calculated) (g/m^3)	7.913	7.754
Absorption coefficient (mm^{-1})	21.527	19.172
F(0 0 0)	752	617
Crystal size (mm^3)	$0.04\times0.03\times0.02$	$0.08\times0.01\times0.01$
Theta range (deg)	4.15–26.98	2.94–29.24
Index ranges	$-9\le h\le 9$	$-11\le h\le 11$
	$-12\le k\le 12$	$-4\le k\le 4$
	$-6\le l\le 6$	$-14\le l\le 14$
Reflections collected	3580	2503
Independent reflections	413 [$R_{int}=0.0200$]	454 [$R_{int}=0.0385$]
Completeness to theta (%)	99.8 at 27.48°	95.0 at 29.24°
Absorption correction	Semi-empirical from equivalents	Semi-empirical from equivalents
Max. and min. transmission	0.6727 and 0.4797	0.8314 and 0.3092
Refinement method	Full-matrix least-squares on F^2	Full-matrix least-squares on F^2
Data/restraints/parameters	413/0/41	454/0/44
Goodness-of-fit on F^2	1.071	1.028
Final R indices [$I>2$sigma(I)]	$R_1=0.0197$, w$R_2=0.0575$	$R_1=0.0230$, w$R_2=0.0480$
R indices (all data)	$R_1=0.0199$, w$R_2=0.0577$	$R_1=0.0322$, w$R_2=0.0507$
Extinction coefficient	0.0133(8)	–
Largest diff. peak and hole (e Å^{-3})	1.470 and −1.094	1.342 and −1.244

Table 2
Atomic coordinates and displacement factors for $CeRh_2O_5$.

	Wyckoff	x	y	z	U_{eq} (Å$^2\times10^{-3}$)[a]
Ce	4*c*	0.7354(1)	3/4	0.1987(1)	4(1)
Rh	8*d*	0.5812(1)	0.4409(1)	0.2493(1)	4(1)
O1	8*d*	0.3314(5)	0.4436(4)	0.0638(8)	5(1)
O2	4*c*	0.6216(8)	1/4	0.0801(11)	8(1)
O3	8*d*	0.4829(5)	0.3767(3)	0.5990(7)	6(1)

[a] U_{eq} is defined as one-third of the trace of the orthogonalized U^{ij} tensor.

Table 3
Atomic coordinates and displacement factors for $Ce_{0.55}Rh_2O_4$.

	Wyckoff	x	y	z	U_{eq} (Å$^2\times10^{-3}$)[a]
Ce[b]	4*c*	0.2353(1)	1/4	0.6609(1)	13(1)
Rh1	4*c*	0.0901(1)	1/4	0.4016(1)	6(1)
Rh2	4*c*	0.4473(1)	3/4	0.3835(1)	7(1)
O1	4*c*	0.3059(6)	1/4	0.3344(4)	7(1)
O2	4*c*	0.4119(6)	3/4	0.5714(4)	7(1)
O3	4*c*	0.5371(7)	3/4	0.2115(4)	13(1)
O4	4*c*	0.8811(6)	1/4	0.4736(4)	7(1)

[a] U_{eq} is defined as one-third of the trace of the orthogonalized U^{ij} tensor.
[b] The occupancy factor for Ce is 0.554(2).

DC electrical conductivity measurements were conducted by a two probe method or four probe method. Seebeck coefficient measurements were conducted over the temperature region 120–300 K. Magnetic measurements at 1.0 T were made using Quantum Design PPMS. Band structure calculations were performed using the linear muffin-tin orbital (LMTO) method with the atomic sphere approximation (ASA) including the combined correction (CC). The LMTO-ASA code used in the calculations was developed in Stuttgart by Andersen et al. [8]. Interstitial space was filled with empty spheres. The k-space integrations employed the tetrahedron method using irreducible k-points within the Brillouin zone. The number of k-points included in the calculations is 196. The Perdew–Wang generalized gradient approximation was used to treat the effects of exchange and correlation [9].

3. Results

Our investigation of the ternary Ce–Rh–O system shown in Fig. 1 revealed the existence of two new ternary compounds, $CeRh_2O_5$ and $Ce_{2/3-x}Rh_2O_4$ ($x\sim0.11$–0.14). In the case of $CeRh_2O_5$ lustrous reddish black crystals several hundred micrometers in length were obtained (Fig. 2). Microprobe analysis of these crystals indicated that impurity elements from the flux or crucible were less than 1%. The structure of $CeRh_2O_5$ is shown in Fig. 3(a), and some bond distances and angles are given in Table 4. This structure is the same as recently reported for $Bi_{2/3}Ce_{1/3}Rh_2O_5$ [10], which has a slightly higher unit cell volume than $CeRh_2O_5$. As shown in Fig. 4(a), Ce cations in the channels have a coordination number of seven. The bond valence sums for Rh and Ce were calculated to be 3.19 and 3.82, respectively, suggesting the formula $Ce^{4+}Rh_2^{3+}O_5$. We used a bond valence parameter, $l_0=1.800$ for Rh^{3+}, which was deduced recently [11]. A notable feature of the $CeRh_2O_5$ structure is the zigzag chains of edge-shared Rh octahedra extending along the c-axis. The same type of chains exist in other structures such as the α-PbO_2 structure [12]. However, this type of zigzag chain has not been observed in other rhodate structures.

The observed electrical conductivity for a single crystal of $CeRh_2O_5$, 4×10^{-8} S/cm at 300 K, indicates that this oxide is a semiconductor. This is consistent with a fully occupied Rh 4d t_{2g} band for Rh^{3+} with LS configuration and supports the formula $Ce^{4+}Rh_2^{3+}O_5$ (Fig. 5). Numerous attempts to synthesize polycrystalline $CeRh_2O_5$ were not successful. Various different temperatures,

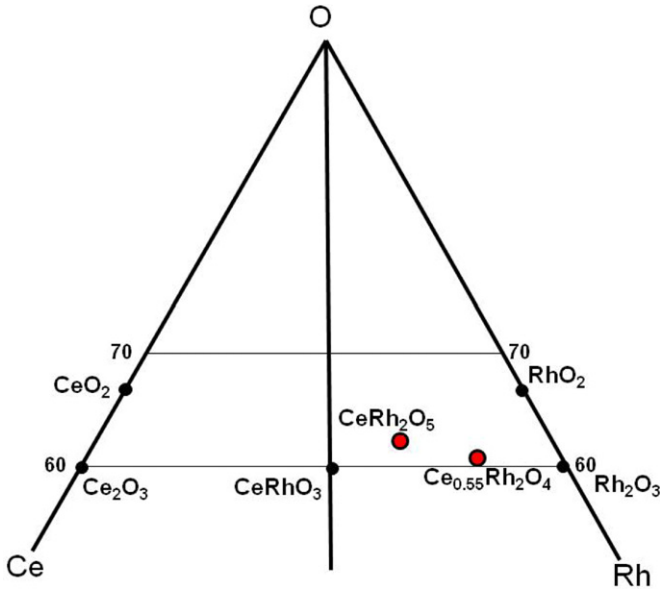

Fig. 1. Ce–Rh–O phase diagram.

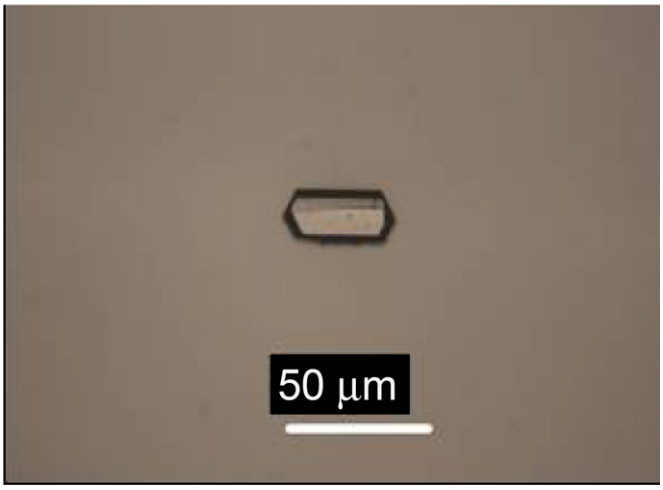

Fig. 2. Flux-grown single crystal of $CeRh_2O_5$.

atmospheres, or fluxes (alkali halides) were employed. No XRD peaks attributable to $CeRh_2O_5$ were ever observed. This failure to produce polycrystalline $CeRh_2O_5$ suggests that the $CeRh_2O_5$ crystals may have been nucleated by very small amounts of impurity as a result of the flux growth.

The calculated electronic band structure and density of states (DOS) for $CeRh_2O_5$ are shown in Fig. 6(a) and (b), respectively. In these figures, the binding energy ($E=0$) is referenced to the valence band maximum. The horizontal axis scale is inversely proportional to the length of the unit cell in various directions. The bands are so flat that the maximum of the valence band and the minimum of the conduction band are unclear, but the band gap is about 1 eV. The antibonding states of the valence band are composed of Rh 4*d* t_{2g} and O 2*p* states. The conduction band is composed of Rh 4*d* e_g and O 2*p* states, but there is a very narrow Ce 4*f* band at the same energy. This Ce 4*f* band is so narrow that it may be considered to be localized Ce 4*f* states. The energy of the Ce 4*f* band cannot be reliably placed by our calculation, and we believe it to be in the gap instead of at the bottom of the valence band. There are no electrons in the Ce 4*f* states; thus, Ce is all Ce^{4+}. Moderate dispersion of bands is seen along the Γ to X direction, since in real space the Γ to X line corresponds to a direction parallel to the *a*-axis, which is the intralayer direction within the Rh_2O_5 layer. At the X, Y, and Z points, degeneracies occur due to the screw axis in this space group.

The $CaFe_2O_4$-type structure of $Ce_{2/3-x}Rh_2O_4$ is shown in Fig. 3b, and some bond distances are given in Table 5. All the oxygen ions have a coordination of three, and double rutile-type chains connect to each other sharing corners to form a Rh_2O_4 framework. The Ce cations reside in the tunnels along the *b*-axis

Table 4
Structural features for $CeRh_2O_5$.

Rh–O distances (Å)	Ce–O distances (Å)	Rh–O–Rh angles (deg)	Rh–Rh distances (Å)
O(1) 2.020(4) 2.026(4) 2.054(4)	O(1) 2.373(4)*2	O(1) 95.89(14)	3.0252(8) 3.0381(8)
O(2) 2.083(2)	O(2) 2.197(6)		
O(3) 2.018(4) 2.004(3)	O(3) 2.245(4)*2 2.420(4)*2	O(3) 98.13(14)	

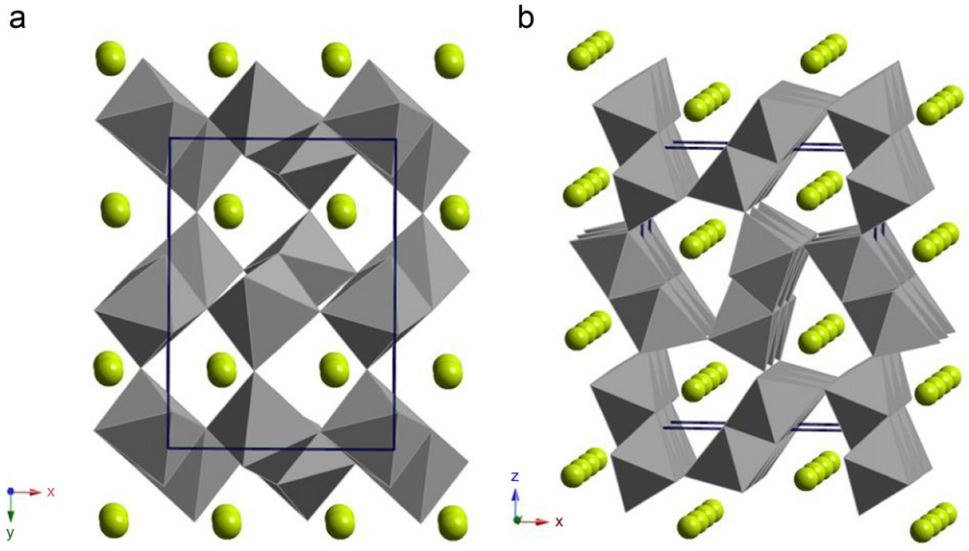

Fig. 3. Crystal structure of (a) $CeRh_2O_5$ and (b) $Ce_{0.55}Rh_2O_4$.

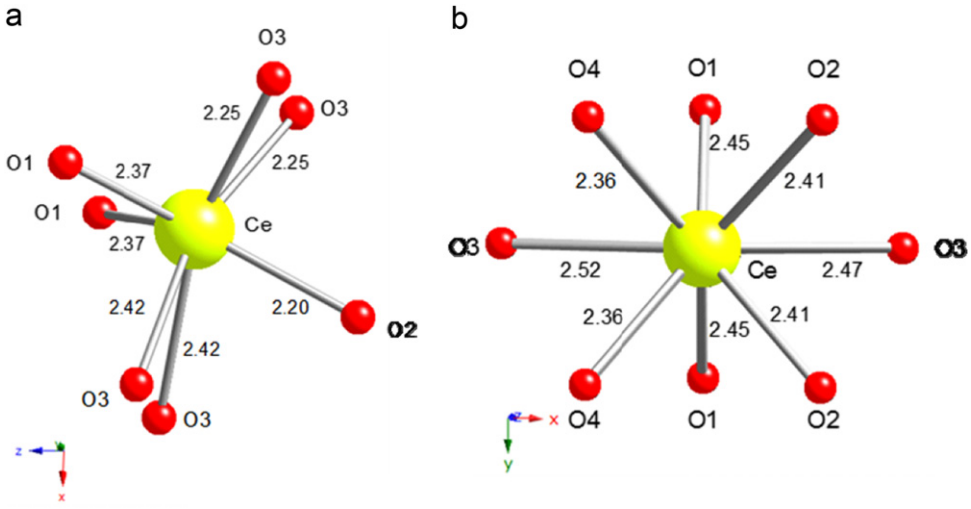

Fig. 4. Local coordination for Ce ion of (a) $CeRh_2O_5$ and (b) $Ce_{0.55}Rh_2O_4$ with bond distances (Å: a view along the tunnel).

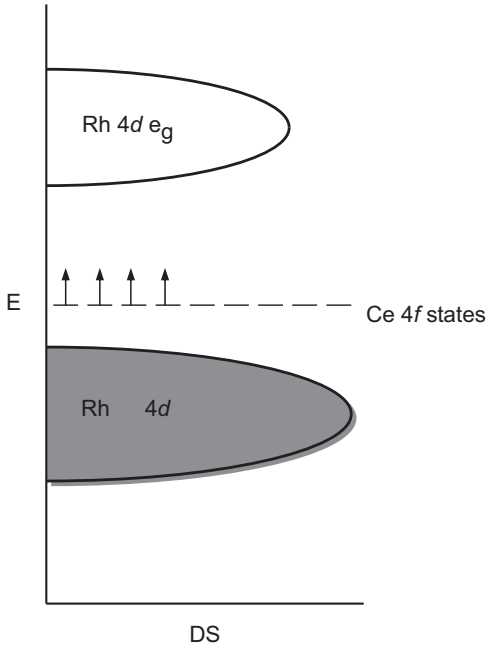

Fig. 5. Schematic energy level diagram where both Rh bands shown have a strong admixture of O 2*p* states. The Ce 4*f* states shown represent one *f* state each for different Ce atoms. Some of these Ce 4*f* states are occupied by one electron as shown for $Ce_{2/3-x}Rh_2O_4$. In the case of $Ce^{4+}Rh_2^{3+}O_5$ the Ce 4*f* states are all empty and they are somewhat higher in the gap.

with a refined site-occupancy of 0.55, and the local Ce coordination is shown in Fig. 4(b).

Fig. 7 gives the temperature dependence of electrical conductivities and Seebeck coefficients for a $Ce_{2/3-x}Rh_2O_4$ pellet, which indicate semiconductive behavior. The plot of $\log \rho$ vs. $1/T$ is not linear, but a nearly linear dependence is found by plotting $\log \rho$ vs. $1/T^{1/2}$. Fig. 8 gives the magnetic susceptibility of a polycrystalline sample of $Ce_{2/3-x}Rh_2O_4$.

4. Discussion

We have previously reported a defect $CaFe_2O_4$-type structure for $R_{2/3-x}Rh_2O_4$ phases, where *R* is Pr, Nd, Sm, Eu, Gd, Ho, Er, Tm, Yb, Lu, or Y [5]. In some cases *R* was partially replaced with Bi. The oxidation states would be 3+ for both *R* and Rh if *x* is 0.0, but such compositions could not be prepared. Thus for compositions actually prepared, the finite value of *x* required some oxidation of either *R* or Rh. A typical composition was $Eu_{0.58}Rh_2O_4$ where the oxidation states are Eu^{3+} and $Rh^{3.13+}$, indicating Rh^{3+}/Rh^{4+} mixed valency. Since CeO_2, rather Ce_2O_3, is the stable oxide of Ce on heating in air, we might then expect that it would be Ce that is oxidized in $Ce_{2/3-x}Rh_2O_4$. Indeed, both the structure and the properties of $Ce_{2/3-x}Rh_2O_4$ indicate that it contains Rh^{3+} and a mixture of Ce^{3+} and Ce^{4+}. The unit cell volumes for $R_{2/3-x}Rh_2O_4$ phases generally increase with the increasing size of *R* [5]. However, the unit cell volume for the Ce phase (296.0–297.7 Å^3) is much smaller than the volumes for the Pr (304.0 Å^3), Nd (303.8 Å^3), and Sm (302.5 Å^3) phases. Although oxidation of either Ce or Rh will give rise to a reduction in size, the impact is much greater for Ce. The ionic radii for Ce (VIII-coordination) are 1.14 and 0.97 Å for Ce^{3+} and Ce^{4+}, respectively, while the ionic radii for Rh (VI-coordination) are 0.665 and 0.60 for Rh^{3+} and Rh^{4+}, respectively [13]. Thus, the smaller unit cell volume is expected for $Ce_{2/3-x}Rh_2O_4$ due to the high Ce^{4+} content. The bond valence sums calculated from the Rh–O distances in Table 5 for Rh1 and Rh2 are 3.13 and 3.07, respectively, are consistent with this formulation. A meaningful bond valence sum cannot be calculated for Ce because of its partial occupancy of its 4*c* site. The electrical conductivity of $R_{2/3-x}Rh_2O_4$ phases with *R*=Y and Eu is about 30 S/cm with very little variation over the measured temperature range of 77–298 K [5]. The conductivity of a $Ce_{2/3-x}Rh_2O_4$ pellet, however, shows a room temperature conductivity slightly less than 1 S/cm at room temperature and dropping to 10^{-4} S/cm at low temperatures (Fig. 7). This low conductivity at low temperatures indicates the Rh 4*d* t_{2g} band is filled, and it must be Ce that is oxidized. Our magnetic susceptibility measurements (Fig. 8) confirm the presence of Ce^{3+}. The amount of Ce^{3+} derived from the data in Fig. 8 is less than that indicated by the $Ce_{0.55}^{3.64+}Rh_2^{3+}O_4$ formula established for a single crystal but is consistent with a formula of $Ce_{0.525}^{3.81+}Rh_2^{3+}O_4$. The refined cell dimensions for the polycrystalline sample are a=9.0050(6), b=3.0544(3), and c=10.7635(6) Å. This gives a cell volume of 296.05(2) Å^3, which is slightly lower than the volume of 297.7(8) Å^3 found for the single crystal. This is consistent with the powder having a larger amount of Ce^{4+} relative to Ce^{3+}.

Mixed valent Ce compounds are well known. Several different oxides occur intermediate between Ce_2O_3 and CeO_2, but they oxidize to CeO_2 on heating in air. However, some oxides

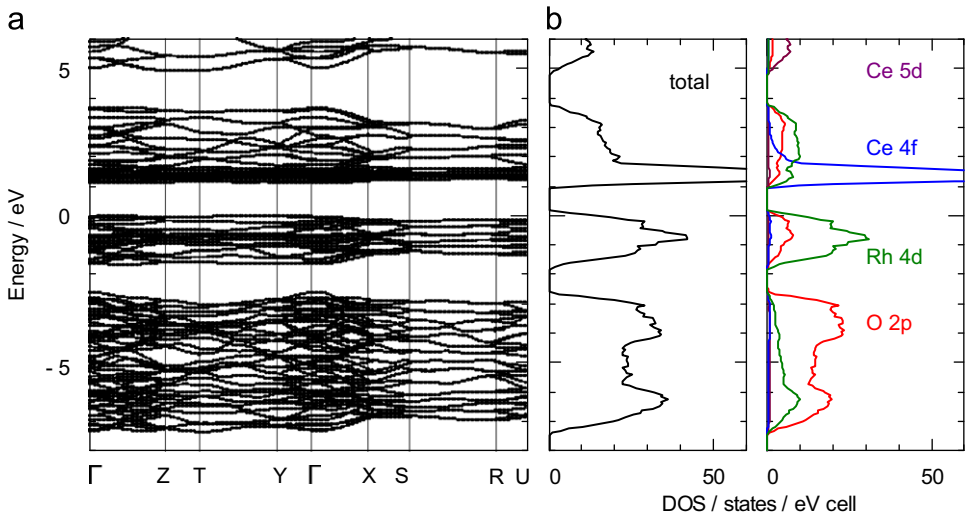

Fig. 6. (a) Calculated band structure for $CeRh_2O_5$. $\gamma=(0, 0, 0)$, $X=(1/2, 0, 0)$, $Y=(0, 1/2, 0)$, $Z=(0, 0, 1/2)$, $S=(1/2, 1/2, 0)$, $U=(1/2, 0, 1/2)$, $T=(0, 1/2, 1/2)$, and $R=(1/2, 1/2, 1/2)$. (b) The total density of states diagram is shown on the left-hand side. The PDOS plots on the right-hand side show contributions of Rh 4*d* (green), Ce 4*f* (blue), Ce 5*d* (violet), and O 2*p* (red). (For interpretation of the references to color in this figure legend, the reader is referred to the web version of this article.)

Table 5
Selected bond distances (Å) for $Ce_{0.55}Rh_2O_4$.

Rh1–O distances (Å)	Rh2–O distances (Å)	Ce–O distances (Å)
O(1) 2.076(6)	O(1) 2.059(4)*2 O(2) 2.045(4)* 2 2.056(5)	O(1) 2.447(5)*2 O(2) 2.409(4)*2
O(3) 2.014(4)*2	O(3) 2.028(6)	O(3) 2.472(7) 2.516(7)
O(4) 2.039(6) 2.054(4)*2		O(4) 2.356(4)*2

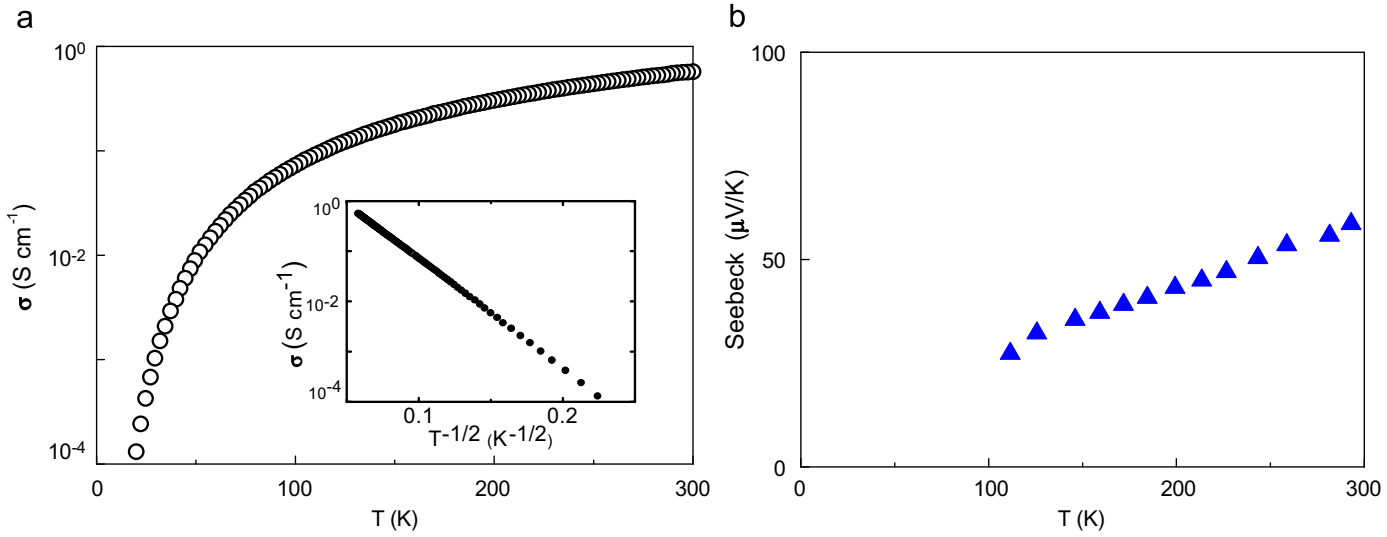

Fig. 7. Temperature dependence of electrical conductivity (a) and Seebeck coefficient (b) for $Ce_{2/3-x}Rh_2O_4$ pellet. The inset shows the $T^{-1/2}$ dependence of the conductivity.

containing Ce^{3+} are resistant to oxidation on heating in air. For example, in the case of $Ce^{3+}PO_4$ and $Ce^{3+}VO_4$ there is essentially no oxidation of Ce^{3+} to Ce^{4+} when heated in air. Thus, it is not surprising that the Ce^{3+} in $Ce_{2/3-x}Rh_2O_4$ does not oxidize to Ce^{4+} on heating in air. The partial occupancy of Ce sites precludes a band structure calculation by our method If the Ce 4*f* states were high in the band gap, n-type conductivity would be expected due to excitations of Ce 4*f* electrons to the conduction band. The observed p-type conductivity indicates that the Ce 4*f* levels are low in the band gap. Excitations from the valence band to empty Ce 4*f* levels then give holes in the valence band.

The simple energy level diagram shown in Fig. 5 can be used to describe the properties of the various rare earth rhodates. For Rh^{3+} oxides such as the $RRhO_3$ perovskites, the Rh 4*d* t_{2g} band is

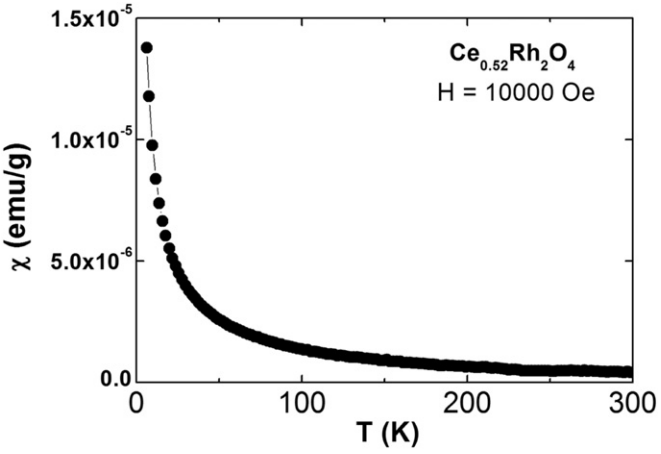

Fig. 8. Magnetic susceptibility for $Ce_{2/3-x}Rh_2O_4$.

filled and the Rh 4*d* e_g band is empty. The band gap is about 1.8 eV. With the Rh^{4+} present in the $R_2Rh_2O_7$ pyrochlores the t_{2g} band is just 5/6 occupied yielding p-type conductors. In general there are no rare earth states within the band gap. Cerium is an exception. Here we could expect Ce 4*f* states in the gap. If the Ce states shown in Fig. 5 are filled we have Ce^{3+}. If they are empty, we have Ce^{4+}. For the $R_{2/3-x}Rh_2O_4$ phases where *R* is not Ce, there are unfilled states at the top of the t_{2g} band in proportion the value of *x*. In the case of $Ce_{2/3-x}Rh_2O_4$ the t_{2g} band is filled and about 18–36% of the Ce 4*f* states are occupied. There will be some conductivity based on Ce 4*f* electrons hopping to empty Ce 4*f* states and Ce 5*d* states. However, the primary contribution to conductivity with increasing temperature is based on excitations from the filled t_{2g} band to the empty Ce 4*f* states that give rise to conductivity from the Rh 4*d* t_{2g} band. The low conductivity of $Ce^{4+}Rh_2^{3+}O_5$ suggests that here the Ce 4*f* states, which are all empty, are located somewhat higher in the band gap. Substitution of Bi^{3+} for Ce^{4+} gives $Bi_{2/3}^{3+}Ce_{1/3}^{4+}Rh_2^{3.3+}O_5$, which produces a phase with metallic properties due to a partially filled Rh 4*d* t_{2g} band [10].

Acknowledgments

We thank Dr. P. Newhouse and Dr. J. Tate (Oregon State University) for experimental support. We also thank Prof. O.K. Andersen, and Dr. O. Jepsen (MaxPlank Institute, Stuttgart, Germany) for providing the LMTO codes and for support. This work was supported by National Science Foundation grant DMR 0804167.

References

[1] H. Müller-Buschbaum, Z. Anorg. Allg. Chem. 633 (2007) 1289.
[2] R.D. Shannon, Acta Crystallogr. B26 (1970) 447.
[3] R.B. Macquart, M.D. Smith, H.-C. zur Loye, Cryst. Growth Des. 6 (2006) 1361.
[4] V.B. Lazarev, I.S. Shaplygin, Mater. Res. Bull. 13 (1978) 229.
[5] H. Mizoguchi, L.N. Zakharov, A.P. Ramirez, W.J. Marshall, A.W. Sleight, M.A. Subramanian, Inorg. Chem. 48 (2009) 204.
[6] G.M. Sheldrick, SHELEXTL, Version 6.14 Bruker Analytical X-ray Instruments, Inc., Madison, WI, 2003.
[7] I.D. Brown, J. Appl. Crystallogr. 29 (1996) 479.
[8] O.K. Andersen, Z. Pawlowska, O. Jepsen, Phys. Rev. B 34 (1986) 5253.
[9] J.P. Perdew, Y. Wang, Phys. Rev. B 33 (1986) 8800.
[10] H. Mizoguchi, A.P. Ramirez, L.N. Zakharov, A.W. Sleight, M.A. Subramanian, J. Solid State Chem. 181 (2008) 56.
[11] H. Mizoguchi, A.P. Ramirez, T. Siegrist, L.N. Zakharov, A.W. Sleight, M.A. Subramanian, Chem. Mater. 21 (2009) 2300.
[12] A.I. Zaslavskii, Y.D. Kondrashev, S.S. Talkachev, Dokl. Akad. Nauk SSSR 75 (1950) 559.
[13] R.D. Shannon, Acta Crystallogr. A 32 (1976) 751.